CORE
Metadata, citation and similar papers at core.ac.uk
Provided by Digital.CSIC

Polarized laser light scattering applied to surface morphology characterization of epitaxial III–V semiconductor layers

M. U. González[a)]
Instituto de Microelectrónica de Madrid (IMM-CNM), Consejo Superior de Investigaciones Científicas, C/Isaac Newton, 8, 28760 Tres Cantos, Madrid, Spain

J. A. Sánchez-Gil
Instituto de Estructura de la Materia, Consejo Superior de Investigaciones Científicas, Serrano, 121, 28006 Madrid, Spain

Y. González and L. González
Instituto de Microelectrónica de Madrid (IMM-CNM), Consejo Superior de Investigaciones Científicas, C/Isaac Newton, 8, 28760 Tres Cantos, Madrid, Spain

E. R. Méndez
División de Física Aplicada, Centro de Investigación Científica y de Educación Superior de Ensenada, Apdo. Postal 2732, Ensenada, Baja California, 22800 México

(Received 12 August 1999; accepted 5 May 2000)

In this paper, we analyze typical morphologies of epitaxial III–V semiconductor layers by using a polarized laser light scattering technique. Crosshatched topographies, which are developed during heteroepitaxial growth, are studied. A sample with an intentionally high density of oval defects is also explored to establish how the laser light scattering pattern is affected by the presence of these defects, which are unavoidable in the epitaxial layers grown by molecular beam epitaxy. The former topographies produce a scattered light pattern that is highly anisotropic, with the intensity concentrated along two preferential directions; the latter defects give rise to a fairly isotropic pattern. Employing a perturbation-theoretical model, whose applicability and consistency are explicitly demonstrated by our results, the surface power spectral density is retrieved from the angle-resolved light scattering experimental data. For the samples exhibiting crosshatched topography, the scattering measurements provide information that allows us to model the roughness of the surface in terms of two quasi-one-dimensional, anisotropic components, and one two-dimensional, isotropic, long-range background. The root mean square heights and the typical lateral distances between ridges are obtained in quantitative agreement with the values extracted from the atomic force microscopy measurements. For the sample presenting oval defects, we consider their contribution to the surface power spectral density by means of a simple model of randomly distributed particles on a surface, and we compare the resulting power spectral density with typical behavior found in the literature for good-morphology GaAs layers. With the help of the *ex situ* information thus obtained, we also discuss the implementation of the light scattering technique for *in situ* monitoring during epitaxial growth. *© 2000 American Vacuum Society.* [S0734-211X(00)04904-0]

I. INTRODUCTION

Epitaxial growth techniques are essential for the fabrication of new and sophisticated electronic devices, such as millimeter and microwave integrated circuits and vertical cavity surface emitting lasers.

The quality of the epitaxially grown structures greatly depends on the deposition parameters, such as substrate temperature, growth rate, and flux ratios. Thus, it is necessary to use real-time control techniques of the epitaxial process. In this situation, the development of *in situ* characterization techniques during growth is crucial. Optical techniques such as dynamic optical reflectance, ellipsometry, differential reflectance spectroscopy, reflectance anisotropy, and light scattering are very powerful tools because they are simple, fast, inexpensive, contact-free, nondestructive and noninvasive, and they do not require vacuum conditions. These techniques can be used in most commonly encountered pressure environments employed in the different epitaxial growth processes.

Laser light scattering (LLS) is an especially interesting technique, due to its sensitivity to surface morphology, which is a critical parameter to obtaining good performance in electronic and optoelectronic devices. Moreover, the monitoring of the surface morphology features that develop during epitaxial growth of different heterostructures provides information about important processes that take place during growth, such as plastic and elastic relaxation, and three-dimensional nucleation, or the formation of quantum dots.

Although the inverse problem in electromagnetic theory is in general a formidable task, it has already been shown that in certain limits the LLS intensity can be related to the mean surface roughness.[1] Under the assumption of smooth rough-

---

[a)] Electronic mail: ujue@imm.cnm.csic.es ness and small slopes, the angular distribution of the scattered intensity can be calculated by means of perturbation theories.[1,2] By retaining the lowest-order term in the expansion of the scattering amplitude in powers of the surface profile function, the resulting scattered intensity can be shown to be proportional to the surface power spectral density (PSD), namely, the Fourier transform of the correlation function of the surface topography. This applies not only to the simplest scattering configuration, consisting of a rough interface separating vacuum (or any other propagating medium) from a semi-infinite, dielectric medium (see Refs. 1–3, and references therein); similar proportionality has been found in the case of a rough film on a planar substrate with different dielectric permittivities,[4–8] and even for multilayer structures.[9,10] The criteria for the applicability of such perturbation-theoretical expressions[1,2,11] for the typical surface roughness developed during epitaxial growth are, in most cases, fulfilled as a result of the high smoothness of the surfaces thus generated. This allows us to use the LLS technique for viewing and studying surface features as small as tenths of nanometer in height and with lateral dimensions larger than λ/2 (Rayleigh limit). It should be mentioned that the latter limit for the optically discernible lateral dimensions can be overcome by using near-field optical microscopy,[12] a technique that unfortunately poses severe difficulties for implementation as a real-time characterization tool.

As demonstrated,[13–17] LLS is a powerful technique for *in situ* monitoring of surface evolution during growth. However, its implementation is complicated by geometrical restrictions imposed by the growth reactor, which does not usually allow obtainment of the full spatial distribution of the scattered intensity. Nevertheless, the time evolution of scattered light at fixed angular positions still yields useful information. Therefore, in order to choose the most appropriate configuration for *in situ* measurements and to achieve a correct interpretation of the results, we have carried out *ex situ* characterization of common surface morphologies that develop during epitaxial growth of III–V systems. Our aims in this paper are to assess the capabilities of the LLS technique to characterize the topography of this kind of systems and to evaluate the validity and utility of the scattering perturbation theory applied to interpret it.

To that end, in Sec. III we present the results from polarized light scattering experiments (the experimental setup being described in Sec. II) of two typical surface topographies developed during epitaxial growth by molecular beam epitaxy (MBE) on (001) III–V semiconductor substrates: the crosshatched surface morphology, and the presence of oval defects. The oval defects are randomly distributed isolated defects, which appear related to two main causes: (i) impurities and particulates on the surface substrate prior to growth, and (ii) liquid-gallium ''spitting'' and gallium oxides coming from the gallium cell during growth.[18] The formation of oval defects in MBE epitaxial layers is inherent to the growth process, although their density can be significantly reduced with state-of-the-art MBE technology. One of the challenges is analyzing the scattered signal due to the presence of this kind of defects, which is convoluted with surface roughness contributing to the LLS signal. The crosshatched morphology (see Ref. 14, and references therein) develops during growth of low-strained heteroepitaxial systems (mismatch $\epsilon_0 < 2\%$) and consists of ripples and troughs aligned along [110] and [110] directions. It is associated with local surface diffusion variations caused by the presence of strain fields related to misfit dislocations formed during plastic relaxation.

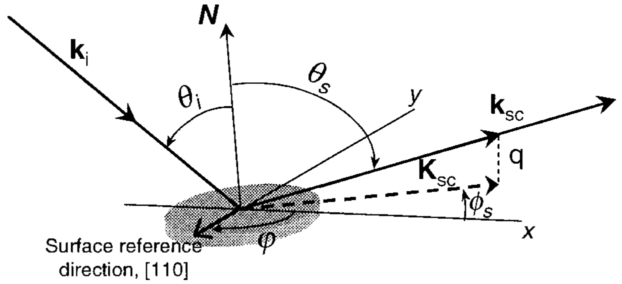

FIG. 1. Schematic of the light scattering geometry for plane-wave incidence.

The LLS experimental data are then evaluated by means of the scattering perturbation theory to obtain the PSDs of the samples under study, providing qualitative and quantitative information of the surface topography; this is discussed in Sec. IV. Finally, our main results (summarized in Sec. V) support the high potential of LLS as an *in situ* characterization technique for monitoring growth.

II. EXPERIMENT

The samples studied in this work consist of 400-nm-thick $In_{0.2}Ga_{0.8}As$ layers grown on GaAs (001) substrates (lattice mismatch $\epsilon_0 = 1.4\%$). One of the layers (sample A) was grown by MBE at a substrate temperature $T_s = 500\,°C$ and the other (sample B) was grown by atomic layer molecular beam epitaxy (ALMBE) at $T_s = 200\,°C$. We have also studied homoepitaxial samples of GaAs on GaAs (001) with different densities of oval defects. Here, we show the results for a 780-nm-thick layer of GaAs grown by MBE at $T_s = 580\,°C$ (sample C), which presents an extremely high density of large oval defects with a broad distribution of lateral size (100 nm$<l<$8 μm) and height (50 nm$<h<$1 μm). The surface morphology of all these layers was studied by polarized laser light scattering and the results were cross-checked with atomic force microscopy (AFM) measurements of the surface topography.

A schematic of the light scattering geometry for plane-wave incidence is shown in Fig. 1. The incident wave vector $\mathbf{k}_i$ and the surface normal $\mathbf{N}$ fix the so-called plane of incidence π_{inc}, whose intersection with the surface plane is taken as the origin for the azimuthal angles. The scattered wave vector direction is determined by the polar, θ_s, and azimuthal, ϕ_s, scattering angles $(-\pi/2 \leq \theta_s \leq \pi/2, -\pi/2 \leq \phi_s \leq \pi/2)$. Only the polar angle of incidence, θ_i, is necessary to determine the incident wave vector direction because of the definition of the origin of azimuthal angles $(\phi_i \equiv 0)$. We have also included the ''surface azimuthal'' angle φ (0

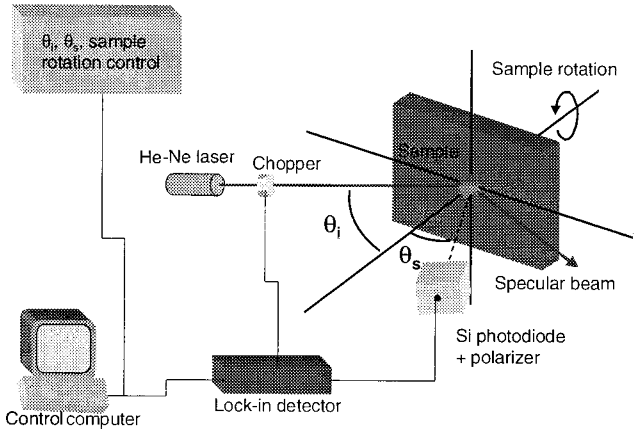

FIG. 2. Experimental setup for the polarized laser light scattering (LLS) measurements. A 10 mW linearly polarized He–Ne laser (λ=633 nm) is used as incident light. The sample is placed in a goniometer that permits us to change the angle of incidence θ_i between 0° and 60°, and the surface azimuthal angle φ between 0° and 360°. Scattered light is collected with a silicon photodiode situated in the plane of incidence π_{inc} and mounted on a rotatable arm that scans between polar scattering angles θ_s of −72° and 72°. We have introduced a polarization analyzer in front of the photodiode to select the polarization of the detected light. We employ lock-in detection to improve the signal-to-noise ratio.

$\leqslant\varphi\leqslant 2\pi$), which accounts for the surface position with respect to the plane of incidence. We define φ as the angle between a reference direction of the surface and the intersection of π_{inc} with the surface plane. We have chosen the [110] direction as the surface reference direction.

Our LLS experimental setup is shown in Fig. 2. We use as incident light a 10 mW linearly polarized He–Ne laser ($\lambda=633$ nm), whose spot on the sample has a diameter of 1 mm. The laser can be rotated to select the beam polarization. The sample is placed on a goniometer, which permits us to change the polar angle of incidence θ_i between 0° and 60°, and the surface azimuthal angle φ between 0° and 360°. The scattered light is collected with a silicon photodiode situated in the plane of incidence; thus $\phi_s=0$ in all our measurements. The photodiode is mounted on a rotatable arm that can move in the plane of incidence, scanning polar scattering angles θ_s from −72° to 72°. In front of the photodiode we have introduced a polarization analyzer to select the polarization of the detected light. It should be pointed out that when θ_s is very close to $(-\theta_i)$, the photodiode blocks the He–Ne laser light; consequently, the backscattering information is not available in our experiments. We employ lock-in detection to reject spurious signals and to improve the signal-to-noise ratio. This setup allows us to carry out two types of measurements: angle-resolved light scattering (ARLS) and azimuthal-dependent light scattering (AzLS).

For the AzLS measurements, we choose the angle θ_i and the polarization of the incident beam, place the photodiode at a fixed polar scattering angle θ_s in the plane of incidence, and rotate the sample to obtain the scattered intensity at different surface azimuthal angles. With this kind of measurements, we can distinguish between isotropic scattering, independent of φ, and anisotropic scattering. In the latter case, these measurements also allow us to identify preferential scattering directions.

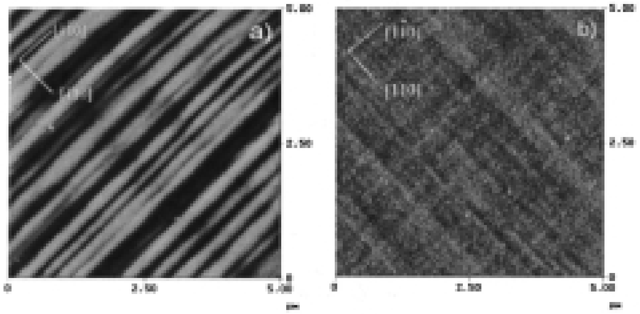

FIG. 3. AFM images of two crosshatched surfaces. (a) Surface of a sample consisting of a 400-nm-thick layer of $In_{0.2}Ga_{0.8}As$ grown by molecular beam epitaxy (MBE) at substrate temperature $T_s=500\,°\text{C}$ on GaAs (001). (b) Surface of a sample consisting of a 400-nm-thick layer of $In_{0.2}Ga_{0.8}As$ grown by atomic layer molecular beam epitaxy (ALMBE) at $T_s=200\,°\text{C}$ on GaAs (001). Both images are printed using the same grayscale.

The other type of measurements we can carry out, ARLS, provides the distribution of scattered light in the plane of incidence. The detector is moved in this plane while keeping constant the polar angle of incidence θ_i, the polarization, and the sample surface azimuthal angle φ. Through a combination of the two main modes of operation of our experimental setup, we can obtain the angular distribution of scattered light for different orientations of the surface. The possibility of changing the surface azimuthal angle φ is of fundamental importance when the surface presents anisotropic roughness. In this work, we performed ARLS measurements at different angles of incidence: $\theta_i=0°$, 10°, 20°, 30°, 40°. We employ both *s*- and *p*-polarized incident light and select the desired polarization of the scattered light through the polarization analyzer placed in front of the detector.

III. EXPERIMENTAL RESULTS

Figure 3 shows the topography, as observed by AFM, of the heteroepitaxial $In_{0.2}Ga_{0.8}As$ on GaAs (001) layers studied in this work. Sample A (grown by MBE at $T_s=500\,°\text{C}$) is shown in Fig. 3(a) and sample B (grown by ALMBE at $T_s=200\,°\text{C}$) is shown in Fig. 3(b). The AFM images are printed using the same grayscale to distinguish changes in the roughness height by a simple visual inspection. Both surfaces present lines along ⟨110⟩ directions, which is characteristic of crosshatched patterns. However, the distinct growth conditions give rise to noticeable differences in their morphologies. The surface in Fig. 3(a) is clearly anisotropic, with ridges along the [110] direction more closely spaced than those oriented along [110]. The height variations are more pronounced along the [110] direction than along the [110] one. In contrast, Fig. 3(b) shows a smoother surface, still anisotropic, but with similar features along these two preferential perpendicular directions. In Table I, we present data corresponding to the ridge height and the distance between consecutive ridges obtained from the AFM measurements. These parameters were obtained by averaging over

TABLE I. Distances and height values for crosshatched roughness in samples A and B obtained from the AFM and LLS measurements. Distances between ridges running along the [110] direction and their height are represented by $d_{[110]}$ and $h_{[110]}$, respectively. Distances and height for features along the [110] direction are represented by $d_{[1\bar{1}0]}$ and $h_{[1\bar{1}0]}$, respectively.

		$d_{[110]}$ (μm)	$d_{[1\bar{1}0]}$ (μm)	$h_{[110]}$ (nm)	$h_{[1\bar{1}0]}$ (nm)
	Sample A	0.71	1.3	17.2±0.5	2.3±0.3
AFM	Sample B	Not defined	Not defined	2.5±0.2	2.1±0.2
	Sample A	0.74	1.15	12	3.2
LLS	Sample B	0.33	0.2	1.8	1.7

the AFM profiles taken along the ⟨110⟩ directions, in a rectangular area of the AFM scans of these samples. We have considered as the characteristic lateral feature on the surface, *d*, the average of the distance between two consecutive peaks. As for the representative feature in the vertical direction, *h*, we have taken the average of the peak-to-valley values.

The typical crosshatched roughness shown in Fig. 3 produces a characteristic pattern of scattered light. Figure 4 shows such an image, taken with a charge-coupled device (CCD) camera. The sample was illuminated with a He–Ne laser under normal incidence, and the scattered light was projected onto a flat screen placed in front of the sample. A circular hole in the screen allowed the illumination of the sample. We observe that the scattered light is strongly concentrated along two orthogonal lines, parallel to the ⟨110⟩ directions, which indicates that crosshatched topography can be envisioned as a superposition of two perpendicular quasi-one-dimensional (quasi-1D) components. The light scattered along each ⟨110⟩ direction comes from the ridges perpendicular to it. By studying the angular distribution of scattered light along those preferential directions we can obtain further information on the surface roughness characteristics.

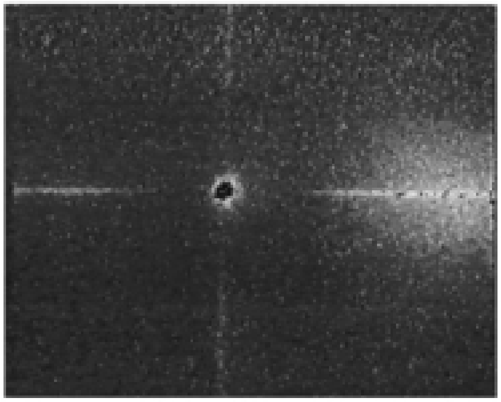

FIG. 4. Light scattered by a crosshatched surface illuminated at normal incidence with a He–Ne laser (λ=633 nm). Image was taken with a CCD camera, projecting the scattered light onto a flat screen situated in front of the sample. A circular hole has been made in the center of the screen to allow the incident beam to reach the sample. The horizontal bright line is parallel to the surface [110] direction and corresponds to light scattered by roughness features perpendicular to it. The vertical bright line comes from features parallel to the [110] direction.

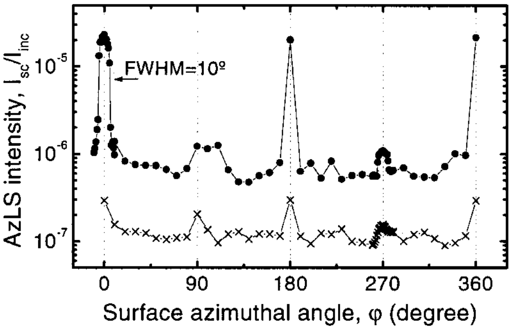

FIG. 5. *s*-polarized scattered intensity during surface azimuthal-dependent light scattering (AzLS) measurements of samples A (●) and B (×). Data were taken under *s*-polarized normal incidence (λ=633 nm) at $\theta_s=30°$. Surface azimuthal angles $\varphi=0°$ and $\varphi=180°$ correspond to the [110] direction in the plane of incidence. Surface azimuthal angles $\varphi=90°$ and $\varphi=270°$ correspond to the [110] direction in the plane of incidence.

In the following paragraphs, we present representative LLS results leading to a useful description of the surface morphology. Figure 5 shows the AzLS measurements, normalized to the incident intensity, of samples A (●) and B (×) taken at normal incidence with *s*-polarized light and the detector placed at $\theta_s=30°$. In both cases, we see that the ⟨110⟩ directions are preferential scattering directions. There are narrow peaks in the scattered intensity in those directions, confirming that the crosshatched morphology has two quasi-1D components along them, as mentioned previously. The full width at half-maximum (FWHM) of the AzLS peaks, calculated from data in Fig. 5, is 10°. From the detector angular aperture, we estimate its value to be about 5°. For sample A, we see that the signal at $\varphi=0°$, 180° is one order of magnitude larger than that at $\varphi=90°$, 270°, revealing that is the [110] direction is rougher than the orthogonal one. From this, we conclude that ridges parallel to the [110] direction are higher than the perpendicular ones. The intensity of the light scattered from sample B, although highly anisotropic, is considerably lower than that from sample A, showing that sample B is smoother. Moreover, in the case of sample B, the fact that the intensity in the two preferential scattering directions is similar indicates that the roughness in these two directions has similar statistical properties.

Figure 6 presents ARLS data of samples A [Figs. 6(a)–6(c)] and B [Figs. 6(d)–6(f)], taken at $\theta_i=0°$ [Figs. 6(a) and 6(d)], $\theta_i=20°$ [Figs. 6(b) and 6(e)], and $\theta_i=40°$ [Figs. 6(c) and 6(f)]. In all cases, the intensity data shown have been normalized to the incident intensity. The signal coming from sample B was very low, and we increased the detector angular aperture in that case; thus, a direct comparison of intensities between the top and bottom graphs is not possible. However, the signal from sample B is still lower than that from sample A and the qualitative discussion provided in the following still holds. Closed symbols correspond to the *s*-polarized scattered signal for *s*-polarized incident light (*s*-to-*s*), and open symbols correspond to *p*-to-*p* scattering. No depolarization in the scattered light was observed for these samples. The experiments were made by detecting the scattered intensity in the plane of incidence when the [110] (■,

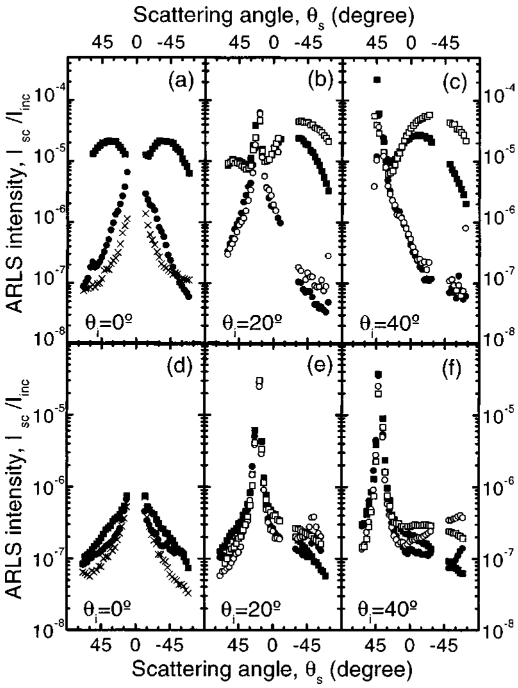

FIG. 6. Angle-resolved light scattered (ARLS) intensity of light (λ=633 nm) scattered by samples A [(a)–(c)] and B [(d)–(f)]. Data correspond to scattered intensity in the plane of incidence when the [110] (■), [110] (●), and [100] (×) surface directions are contained in it. Measurements were taken at θ_i=0° [(a), (d)], at θ_i=20° [(b), (e)], and at θ_i=40° [(c), (f)]. Closed symbols: *s*-polarized incident and scattered light. Open symbols: *p*-polarized incident and scattered light. In both cases, intensity data have been normalized to the incident power. Direct comparison between top and bottom figures is not possible because the detector angular aperture in measurements from sample B was increased due to the low level of signal.

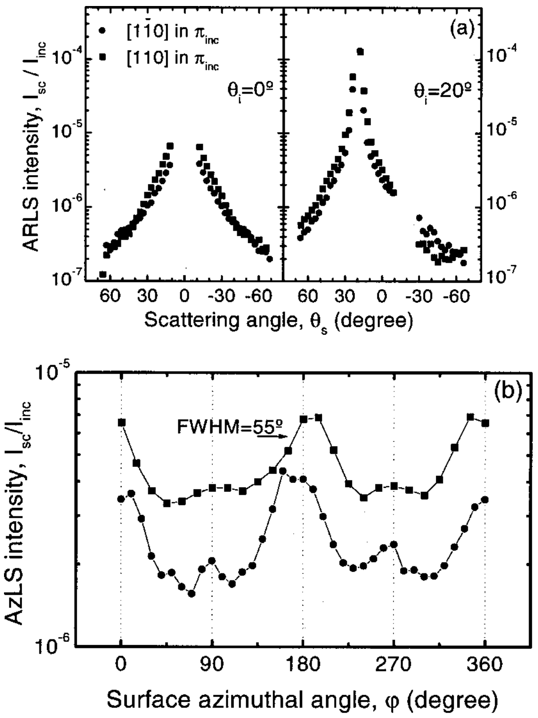

FIG. 7. *s*-polarized light intensity scattered from sample C, which presents a high density of oval defects, illuminated with *s*-polarized light (λ=633 nm). (a) Angle-resolved light scattering (ARLS) data: θ_i=0° (left graph) and θ_i=20° (right graph), for the [110] (■) and [110] (●) directions on $\pi_{\rm inc}$, respectively. (b) Azimuthal-dependent light scattering (AzLS) measurements detected at θ_s=12° for θ_i=0° (■) and at θ_s=30° for θ_i=10° (●).

□), [1$\bar{1}$0] (●, ○), and [100] (×) surface directions are contained in it; we thus obtained the distribution of scattered light both in the preferential scattering directions ([110] and [110]) and in an intermediate one ([100]). As mentioned previously, the light scattered in the plane of incidence when each of the ⟨110⟩ directions are contained in it comes from the surface ridges running along the perpendicular direction. Similar to the AzLS data, from the ARLS data we observe that the scattered light signal for both samples is mainly concentrated on the ⟨110⟩ directions because of the crosshatched nature of the surface. All ARLS data show that sample A scatters more than sample B, indicating that the former is rougher. For sample A, the intensity coming from features along the [110] direction ([110] direction on $\pi_{\rm inc}$) is higher, and this means that the height variations are larger than in the orthogonal direction. In the case of sample B, we can conclude that the features are similar in both directions. On the other hand, we observe that although the scattered intensities obtained under different incidence conditions indeed differ, they allow us to extract the same qualitative results.

Figure 7 corresponds to light scattering data, normalized to the incident intensity, from sample C (GaAs on GaAs (001) grown by MBE at T_s = 580 °C), whose main morphological characteristic consists of the presence of a huge density of oval defects on a flat GaAs homoepitaxial layer. Figures 7(a) and 7(b) show ARLS and AzLS intensity, respectively. The *s*-polarized scattered intensity data in Fig. 7(a) were taken in the plane of incidence under *s*-polarized illumination, with θ_i=0° (left graph) and θ_i=20° (right graph), for the two ⟨110⟩ directions. The curves for other surface azimuthal angles are similar to these, indicating that sample C shows nearly isotropic roughness.

AzLS measurements presented in Fig. 7(b) were done under *s*-polarized incidence, detecting the *s*-polarized scattered signal at θ_s=12° for θ_i=0° (■) and at θ_s=30° for θ_i = 10° (●). We see that the signal has a small dependence on the azimuthal angle φ, and it shows broad peaks (FWHM =50°). These broad peaks, centered at φ=0° and 180°, could indicate that the defects have a tendency to be elongated along the [110] direction. It is clear that these peaks are not as sharp as those found in the case of the crosshatched surfaces (where FWHM<10°) and cannot be related to quasi-1D morphological components. We have not observed depolarization in the light scattered from this sample either.

Using the AzLS technique, we have characterized homoepitaxial GaAs layers with different density and size distribution of oval defects. Although the AzLS plots of these samples are not shown in this work, it is important to note that we always observe broad peaks (FWHM≈50°) centered at φ=0° and 180° (while the level of the LLS signal is characteristic of each sample).

It is obvious that oval defects and crosshatched morphology coexist in low-strained heteroepitaxial MBE samples.

However, we can assume that these two kinds of topographies are not correlated because they originate by different and independent processes: the presence of stress fields in the surface for the crosshatch, and contamination of the substrate or liquid gallium splitting for the oval defects.

The existence of two different and uncorrelated types of roughness on a surface results in a scattered signal that is the sum of light scattered by each type of roughness. Because the presence of a high density of oval defects on a surface considerably increases the amount of scattered intensity, it may mask the scattered signal coming from other types of roughness on our surface. When we try to detect the evolution of a highly anisotropic roughness during growth (as, for example, a crosshatched surface) and we detect an increasing of the scattering signal along the [110] or $[\bar{1}10]$ directions, we must confirm that the signal really corresponds to that kind of anisotropic morphology by means of AzLS measurements: we can test whether we obtain a sharp distribution of the signal with the azimuth or not. If signal distribution is broad, it could mean that we are merely detecting the signal coming from oval defects on the surface.

The high anisotropy of the AzLS measurements of samples A and B (see Fig. 5) allows us to ensure that the LLS signal detected from these samples is coming from crosshatched features. The LLS signal level due to oval defects in these samples is low enough to be masked by the crosshatched LLS signal.

Our *ex situ* LLS experimental results allow us to identify the type of surface morphology, as well as the relative height of surface features. In Sec. IV we will show that, by using a perturbative scattering theory, we can recover the surface PSDs, thus acquiring quantitative information on the surface that helps us to determine the size of the typical surface features.

In situ implementation of the LLS technique has, as mentioned before, several geometrical constraints that must be considered to obtain the whole spectrum of the ARLS characterization. However, *in situ* recording of the AzLS data for fixed θ_i and θ_s only requires the ability to change the azimuthal surface angle; this is a common feature of sample holders in epitaxial growth systems. From our experimental *ex situ* AzLS results, we know that these kind of measurements provide key information about the degree of isotropy of the sample morphology, which is essential to assess the characteristics of the evolution of the growth front in real time.

IV. SURFACE TOPOGRAPHY FROM ANGLE-RESOLVED LIGHT SCATTERING

The question now arises as to how the ARLS distributions relate to the surface topography. Although the inverse problem cannot be solved in a general manner, there exist certain ranges of the scattering parameters for which relevant information can be extracted from the ARLS data.[1,2] Under the assumption of smooth roughness and small slopes, the electric field amplitude (actually, the scattering amplitude, which is related to the electric field through a Rayleigh expansion) can be expanded in powers of the surface profile function.[2] Basically, we consider a heteroepitaxial system as an interface separating vacuum from a homogeneous, isotropic, semi-infinite dielectric medium (characterized by the dielectric permittivity ϵ). The surface profile function, assumed to constitute a realization of a stationary random process, is denoted by $\zeta(\mathbf{r})$. This function is chosen in such a way that it is a zero-mean function, that is, $\overline{\zeta(\mathbf{r})}=0$. The surface height correlation $W(|\mathbf{r}|)$ is defined by

$$\left\langle \zeta(\mathbf{r})\zeta(\mathbf{r}')\right\rangle=\chi^2 W(|\mathbf{r}-\mathbf{r}'|), \tag{1}$$

where the angular brackets here denote an average over the ensemble of realizations of the surface profile function, and $\chi=\langle\zeta^2(\mathbf{r})\rangle^{1/2}$ is the rms height of the surface. At this stage, it is convenient to introduce the Fourier integral representation of $\zeta(\mathbf{r})$,

$$\zeta(\mathbf{r})=\int_{-\infty}^{\infty}\frac{d\mathbf{K}}{(2\pi)^2}\hat{\zeta}(\mathbf{K})\exp(i\mathbf{K}\cdot\mathbf{r}), \tag{2}$$

which also represents a zero-mean random process with the property

$$\langle\hat{\zeta}(\mathbf{K})\hat{\zeta}(\mathbf{K}')\rangle=(2\pi)^2\delta(\mathbf{K}+\mathbf{K}')\chi^2 g(|\mathbf{K}|), \tag{3}$$

where $g(|\mathbf{K}|)$, the power spectral density of the surface roughness, is defined in terms of the surface height autocorrelation function $W(|\mathbf{r}|)$ by

$$g(|\mathbf{K}|)=\int_{-\infty}^{\infty}d\mathbf{r}\,W(|\mathbf{r}|)\exp(i\mathbf{K}\cdot\mathbf{r}). \tag{4}$$

The angular distribution of diffusely scattered intensity normalized to the incident power (also known as the diffuse component of the mean differential reflection coefficient) can be written to lowest order in the rms surface height χ as

$$I_{\alpha\beta}(\mathbf{K}_{\mathrm{sc}})=f_{\alpha\beta}(\mathbf{K}_{\mathrm{sc}},\mathbf{K}_i)g(\mathbf{K}_{\mathrm{sc}}-\mathbf{K}_i)+O\left[\left(\frac{\chi}{\lambda}\right)^4\right]. \tag{5}$$

The scattered wave vector is (see Fig. 1)

$$\begin{aligned}\mathbf{k}_{\mathrm{sc}}&\equiv(\mathbf{K}_{\mathrm{sc}},q)\\&=(2\pi/\lambda)(\sin\theta_s\cos\phi_s,\sin\theta_s\sin\phi_s,\cos\theta_s),\end{aligned} \tag{6}$$

where θ_s and ϕ_s are the polar and azimuthal scattering angles; thus, $\mathbf{K}_{\mathrm{sc}}$ is the component parallel to the *xy* plane, and q is the component perpendicular to the *xy* plane. The incident wave vector $\mathbf{k}_i$ is defined analogously, choosing $\phi_i\equiv 0$ without loss of generality. In this way, $\mathbf{K}_i$ is the component parallel to the *xy* plane for the incident wave vector. Notice the difference between ϕ_s and the surface azimuthal angle φ, which is defined in order to describe the position of the different (001) surface directions with respect to the plane of incidence (see Fig. 1). In Eq. (5), the factor $f_{\alpha\beta}$ is defined as[3]

$$\begin{aligned}&f_{\alpha\beta}(\mathbf{K}_{\mathrm{sc}},\mathbf{K}_i)\\&\quad=\left(\frac{2\pi}{\lambda}\right)^4\frac{|\epsilon-1|^2}{4(2\pi)^2}\cos^{-1}\theta_i\,|\sigma_{\alpha\beta}(\mathbf{K}_{\mathrm{sc}},\mathbf{K}_i)|^2,\end{aligned} \tag{7}$$

where α and β denote the polarization state (s,p) of the scattered and incident light, respectively, in such a way that

$$\sigma_{ss}(\mathbf{K}_{\mathrm{sc}},\mathbf{K}_i)=T_s(\mathbf{K}_{\mathrm{sc}})T_s(\mathbf{K}_i)\cos\phi_s, \tag{8a}$$

$$\sigma_{sp}(\mathbf{K}_{\mathrm{sc}},\mathbf{K}_i)=T_s(\mathbf{K}_{\mathrm{sc}})T_p(\mathbf{K}_i)\sin\phi_s\frac{(\epsilon-\sin^2\theta_i)^{1/2}}{\epsilon^{1/2}}, \tag{8b}$$

$$\sigma_{ps}(\mathbf{K}_{\mathrm{sc}},\mathbf{K}_i)=T_p(\mathbf{K}_{\mathrm{sc}})T_s(\mathbf{K}_i)\sin\phi_s\frac{(\epsilon-\sin^2\theta_s)^{1/2}}{\epsilon^{1/2}}, \tag{8c}$$

$$\sigma_{pp}(\mathbf{K}_{\mathrm{sc}},\mathbf{K}_i)=T_p(\mathbf{K}_{\mathrm{sc}})T_p(\mathbf{K}_i)[\sin\theta_s\sin\theta_i-\epsilon^{-1}\cos\phi_s(\epsilon-\sin^2\theta_s)^{1/2}(\epsilon-\sin^2\theta_i)^{1/2}] \tag{8d}$$

and the Fresnel transmission coefficients T_α are given by

$$T_s(\mathbf{K}_{\mathrm{sc}})=\frac{2q}{q+(\epsilon|\mathbf{k}_{\mathrm{sc}}|^2-|\mathbf{K}_{\mathrm{sc}}|^2)^{1/2}}, \tag{9a}$$

$$T_p(\mathbf{K}_{\mathrm{sc}})=\frac{2\epsilon^{1/2}q}{\epsilon q+(\epsilon|\mathbf{k}_{\mathrm{sc}}|^2-|\mathbf{K}_{\mathrm{sc}}|^2)^{1/2}}. \tag{9b}$$

Because $f_{\alpha\beta}$ depends only on the geometry of the experiment and on the bulk properties of the sample (ϵ), Eq. (5) shows that ARLS data are proportional to the PSD of the illuminated region. In fact, it can be shown that similar perturbative expressions are obtained for multilayer structures,[4–7,9,10] the differences being accounted for by the function $f_{\alpha\beta}$. As we will see in the following, for our purposes the semi-infinite medium assumption suffices. This can be justified on the basis of the optical behavior of the heteroepitaxial systems being studied. Namely, the light reflected back into vacuum from the layer/substrate interface is negligible, as a result of the strong light absorption within the upper layer and the small reflection coefficient at these interfaces due to low index mismatch. However, for smaller epilayer thicknesses (for our heteroepitaxial system $d \leqslant 50$ nm), slight interference effects in the scattered light can be observed, indicating that further refinements of the model should be included to account for the presence of thin layers. Incidentally, we would like to point out that no volume scattering effects stemming from the presence of bulk defects are considered, since no such defects are expected in the type of samples being studied here. If bulk defects were abundant, their contribution to the LLS, and in turn its correlation with the surface scattering contribution, would have to be taken into account. For weak scatterers, this could be done through the first Born approximation, for example, whereas strong scatterers would notably complicate the formalism, possibly making LLS useless as a surface morphology characterization tool.

We will now analyze the experimental ARLS results of Sec. III, exploiting the analytical expression (5). Nonetheless, recall that, inasmuch as the available (detectable) incident and scattered wave vector components are limited in the far field, this technique fails to provide information on roughness lateral dimensions smaller than λ/2 (Rayleigh limit). This is explicitly demonstrated in Eq. (5) through the maximum spatial frequency appearing in the argument of the PSD. In addition, there is another constraint in our ARLS measurements, namely, the absence of data points near the backscattering direction (as seen in Figs. 6 and 7); this is because the light detector in our sample experimental setup blocks the incident light at such angles. On the other hand, the lack of cross-polarized scattering in the plane of incidence mentioned in Sec. III, predicted by Eqs. (5)–(9b), comes in support of our retaining only the lowest-order term in the perturbation theory.

A. Crosshatched surface morphology

Considering the typical shape of the scattering pattern produced by the crosshatched (CH) surfaces (see Fig. 4) and the relation between the PSD and the scattering pattern [given by Eq. (5)], it is natural to assume that the surface roughness basically contains three random and independent components: two quasi-1D components along the [110] and [110] directions (denoted as the *x* and *y* directions, respectively) and a small two-dimensional (2D) isotropic component. The latter is revealed by our ARLS results in directions other than the ⟨110⟩ ones. There is no correlation between the 2D component and either of the quasi-1D ones. The resulting surface roughness profile can be written as follows:

$$\zeta_{\mathrm{CH}}(\mathbf{r})=\zeta_{[110]}(x)+\zeta_{[1\bar{1}0]}(y)+\xi(\mathbf{r}), \tag{10}$$

where, as we mentioned, the three components are assumed to be statistically independent. The PSD thus yields

$$g_{\mathrm{CH}}(\mathbf{K})=2\pi[g^{\mathrm{1D}}_{[110]}(K_x)\,\delta(K_y)+g^{\mathrm{1D}}_{[1\bar{1}0]}(K_y)\,\delta(K_x)]+g^{\mathrm{2D}}(|\mathbf{K}|). \tag{11}$$

With the aim of calculating all components, we have carried out ARLS experiments, as described in Sec. III, along the [110] and [110] directions for different angles of incidence θ_i. From the ARLS distributions thus obtained, and using Eq.(5) with $\phi_s=0$ (scattering signal always in the plane of incidence), the PSDs along the two relevant perpendicular directions are calculated. However, care must be taken when extracting the 1D and 2D components of the PSD, because they involve different normalization of the ARLS data. The procedure is as follows.

First, the complete PSD is retrieved from the ARLS data along the ⟨110⟩ directions. A careful analysis of this function allows the identification of two different behaviors: one corresponding to the low-spatial-frequency part, and the other to the rest of the frequency range. The low-spatial-frequency region coincides in both ⟨110⟩ directions and can thus be identified as the 2D isotropic component. (Alternatively, the ARLS data along the [100] direction could be used for the calculation of this PSD component, which in our case led to similar results, as expected.) This region of spatial frequencies in the ARLS data is normalized to the solid angle $\Delta\Omega_s$ covered by the detector, and it is then fitted (if possible) to an appropriate PSD. We have obtained reasonable agreement with the following function:[9]

$$g^{\mathrm{2D}}(|\mathbf{K}|)=\frac{2\pi\chi_L^2a_L^2}{(1+a_L^2|\mathbf{K}|^2)^{3/2}}, \tag{12}$$

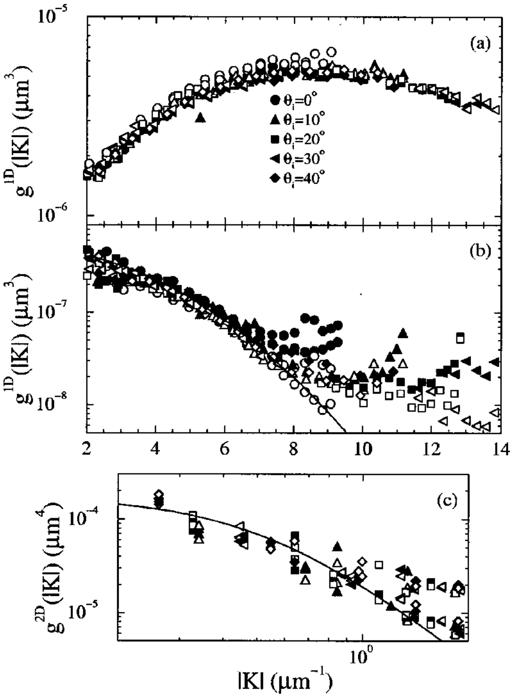

FIG. 8. Power spectral density (PSD) for sample A calculated from angle-resolved light scattering (ARLS) data at different angles of incidence, as those shown in Figs. 6(a)–6(c). Closed symbols: *s*-polarized incident and scattered light. Open symbols: *p*-polarized incident and scattered light. Solid curves are fits to particular functions. (a) 1D PSD along the [110] direction. (b) 1D PSD along the [110] direction. (c) 2D PSD, assumed isotropic, along both directions.

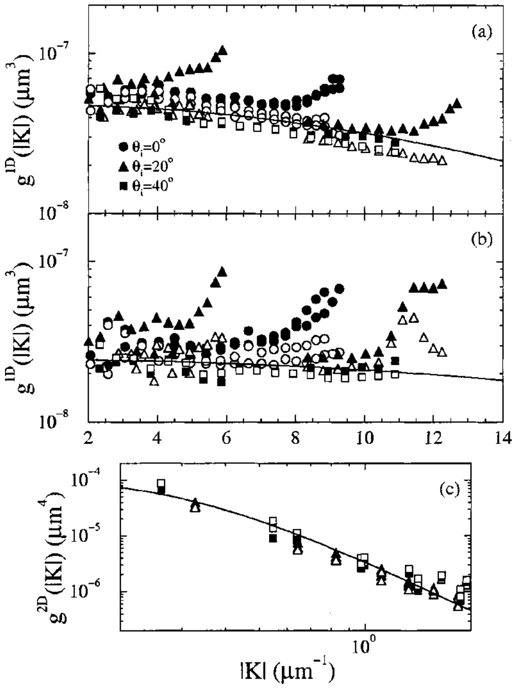

FIG. 9. Power spectral density (PSD) as in Fig. 8, but for sample B [calculated from angle-resolved light scattering data, as those shown in Figs. 6(d)–6(f)].

with a_L and χ_L denoting, respectively, the long-range correlation length and rms height, resulting from a negative exponential surface correlation function.

Next, we subtract this component from the ARLS data and renormalize them by the scattering angle $\Delta\theta_s$ subtended by the detector in the plane of incidence. In this manner, because the detector width in the direction perpendicular to the plane of incidence has been chosen so that it entirely covers the narrow lines of the crosshatched scattered pattern (see Fig. 4), we can formally integrate the PSD along that perpendicular direction. Therefore, even though strictly speaking the expected 1D contribution to the scattered signal is not a delta function as assumed for the PSD model in Eq. (11), the resulting integral can be considered completely equivalent.

The PSD components thus retrieved from the ARLS data are presented in Fig. 8 for sample A and Fig. 9 for sample B. Before analyzing the results in detail, we note that, as expected, there is good agreement between the PSDs obtained from the ARLS data corresponding to the two polarizations and various angles of incidence; this supports the analysis based on the perturbation-theoretical expression (5). The PSD points originating in the region of weak ARLS signals (at large scattering angles) are subjected to larger relative errors, and thus manifest some inconsistencies.

Having a reliable method for obtaining the PSDs, we can extract quantitative information of the surface roughness. Let us first focus on sample A (Fig. 8). The most relevant feature is the broad maximum of the PSD along the [110] direction [see Fig. 8(a)] at $|\mathbf{K}|=8.5\ \mu\text{m}^{-1}$. Roughly speaking, this can be associated with a pseudoperiodicity along the [110] direction with average period $d_{[110]}=2\pi/|\mathbf{K}|=740$ nm. The height of these pseudoperiodic ridges can be estimated by exploring the following property of the PSD:

$$\int \frac{dK^n}{(2\pi)^n}\, g^{nD}(\mathbf{K})=\chi^2, \quad n=1,2. \tag{13}$$

Thus, by integrating the PSD in Fig. 8(a) (including the negative frequencies), the square of the rms height is obtained. Our data yield $\chi_{[110]}=4.3$ nm. If one assumes that the profile is sinusoidal, this rms height is related to the peak-to-valley value $h_{[110]}=2^{3/2}\chi_{[110]}=12$ nm. On the other hand, the PSD along the [110] [see Fig. 8(b)] is basically structureless, with only a monotonic decay with increasing spatial frequency. The fact that no structure can be found along the [110] does not imply that there is no information on the surface. It merely indicates that the 1D roughness component along the [110] is more strongly randomized and weaker in magnitude than the perpendicular component (as revealed by the overall magnitude of the PSDs). Furthermore, we have found that the PSD fits reasonably well the Gaussian correlation function [solid curve in Fig. 8(b)]:

$$g_{[1\bar{1}0]}(K_y)=\pi^{1/2} a \chi^2_{[1\bar{1}0]} \exp\left(-\frac{a^2K_y^2}{4}\right), \tag{14}$$

with $a=450$ nm and $\chi_{[1\bar{1}0]}=0.8$ nm. $\chi_{[1\bar{1}0]}$ is the rms height associated with this roughness component, and in the case of a Gaussian model it is related to the average peak-to-valley heights through the relation $h=4\chi$. The parameter a is called the transverse correlation length and represents the $1/e$ value of the correlation function. For a Gaussian random process, the correlation length can be related to the mean distance between consecutive valleys or ridges of the profile through[19] $\langle d \rangle = 2.56a$, which leads to $\langle d_{[1\bar{1}0]} = 1.15$ μm. We point out, however, that the latter parameter is analogous to, but different from, the pseudoperiod found along the [110] direction, because the roughness along the $[1\bar{1}0]$ decorrelates more rapidly and has no remnants of periodicity.

Finally, the 2D isotropic component of the PSD is shown in Fig. 8(c) for our two main perpendicular directions, along with the fit (solid curve) to the long-range function (12), with $a_L = 1.8$ μm and $\chi_L = 2.9$ nm. Note, in Fig. 8(c), that for spatial frequencies beyond $|\mathbf{K}| = 1$ μm^{-1}, as the strong pseudoperiodic 1D component builds in, there is a slight departure of the PSD data from the fit to the long-range function (12) along the [110] direction. With respect to this 2D component, it should be pointed out that its contribution to the total PSD again exceeds that of the 1D short-range Gaussian function for $|K| > 10$ μm^{-1}, which could be the origin of the spurious PSD data shown in Fig. 8(b) for such spatial frequencies.

The scattering pattern produced by sample B is not quite as well developed along the two orthogonal directions as the one produced by sample A, although one can still find two preferred directions along which the roughness appears. The PSDs shown in Fig. 9, extracted from the ARLS as mentioned previously, look quite similar for both the [110] and the $[1\bar{1}0]$ directions; they follow a monotonic decrease with increasing spatial frequency. Thus, a strongly randomized component along both perpendicular directions is present, and both PSDs can be fitted to the above-mentioned Gaussian model in Eq. (14). Because the decay of the PSDs is slower than that of sample A along $[1\bar{1}0]$, smaller correlation lengths are inferred: $a_{[110]} = 130$ nm and $a_{[1\bar{1}0]} = 78$ nm, with similar rms heights, $\chi_{[110]} = 0.46$ nm and $\chi_{[1\bar{1}0]} = 0.42$ nm, respectively. Nevertheless we note that, particularly along the $[1\bar{1}0]$ direction, the fit is not very accurate, even if the data corresponding to large scattering angles, where the ARLS signals are weak, are eliminated. This is related to the Rayleigh limit, because the region over which the scattering data are available does not permit the retrieval of spatial frequencies corresponding to details smaller than about half a wavelength. Thus, the retrieval of correlation functions with correlation lengths significantly smaller than the wavelength becomes very difficult; the Gaussian exponential decay predicted by the PSD in Eq. (14) is not observable in such a case. Actually, the results in Fig. 9(b) could be fitted to a different PSD, but poor accuracy with respect to the spatial frequency decay would be obtained whatever its particular shape. On the other hand, concerning the 2D isotropic component, good agreement is found [see Fig. 9(c)] with the PSD in Eq. (12) for $a_L = 3.2$ μm and $\chi_L = 1.4$ nm.

All of these features are summarized in Table I, and they agree quite well with the AFM topographical images shown in Fig. 3 and the resulting parameters included in Table I. With regard to sample A, the pseudoperiodicity along the [110] direction accounts for the large ridges running parallel to the $[\bar{1}10]$ direction, whereas the Gaussian correlation function along the latter direction describes the weaker random fluctuations along the ridges that decorrelate more rapidly. The weaker crosshatched pattern of sample B predicted from ARLS is also in agreement with AFM data. Furthermore, although less relevant for our purposes, our optically retrieved PSDs can yield long-range information that is absent from the AFM image.

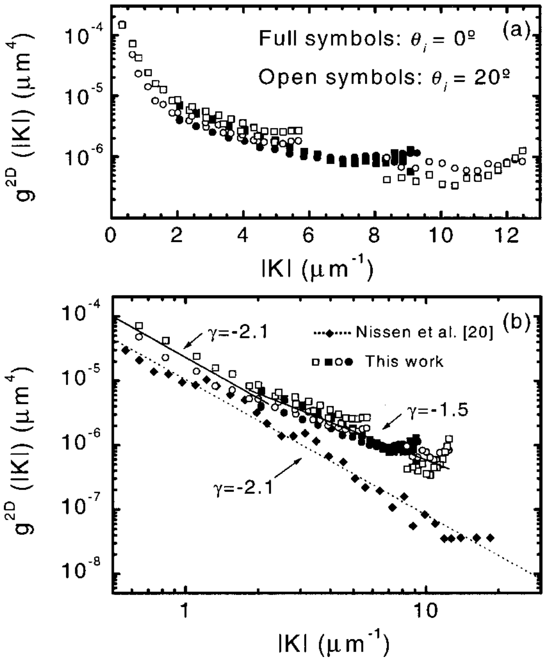

FIG. 10. (a) 2D power spectral density (PSD) for sample C calculated from the angle-resolved light scattering (ARLS) data at two angles of incidence shown in Fig. 7(a) (*s*-polarized incident and scattered light). (□): PSD calculated from ARLS measurements taken with the [110] direction in π_{inc}; (○): PSD from the $[1\bar{1}0]$ direction. (b) Log–log plot of sample C PSD, fitted to two straight lines (—): one of slope $\gamma = -1.5$ in the high-spatial-frequency range and the other of slope $\gamma = -2.1$ for low frequencies. Data from Ref. 20 and their corresponding linear fit (---) have also been plotted for comparison.

B. Presence of oval defects

A similar analysis of crosshatched topography can be made on other kinds of samples. We have performed such a study on sample C, consisting of 780 nm of homoepitaxial GaAs with an extremely high density of randomly distributed oval defects, with a broad dispersion of lateral size (100 nm$<l<$8 μm) and height (50 nm$<h<$1 μm), as observed through AFM and Normarsky measurements.

First of all, as described in Sec. III, from AzLS and ARLS data (Fig. 7) we conclude that there are no quasi-1D roughness components, in spite of the weak anisotropy in scattered intensity with surface azimuthal angle. So, the surface PSD consists of a 2D component, which can be directly calculated through expression (5) with the ARLS data properly normalized by the incident power and the solid angle $\Delta\Omega_s$. The PSD thus obtained is shown in Fig. 10(a). It can be seen that the measured light anisotropy does not imply significant differences in the PSD when calculated from the [110] (■,□) and [110] (●,○) directions, confirming again that surface roughness is nearly isotropic.

As mentioned in Sec. IV A, the integral of the PSD yields the square of the rms height. In the case of the PSD data in Fig. 10(a), this 2D integral gives: $\chi_{2\mathrm{D}} = 3.9$ nm. This value can be compared to those found in the literature for light scattering measurements of good-quality GaAs epilayers grown on GaAs (001).[20,21] This means that, although sample C presents a huge density of oval defects, most of its surface area is flat (free of oval defects), not causing any significant increase of the LLS signal.

In Fig. 10(b), we show a log–log plot of the PSD obtained for this sample with a high density of oval defects. Data corresponding to the low-frequency part can be fitted to a linear behavior with a slope $\gamma = -2.1$, which is the characteristic behavior of the PSD from GaAs grown under good growth conditions, as reported in the literature.[20,22] Data from Ref. 20 are plotted in Fig. 10(b) for comparison. However, for high frequencies the PSD of sample C departs from this behavior, and the experimental data fit to a straight line with slope $\gamma = -1.5$ on a logarithmic scale.

The latter behavior could be explained by taking into account the simple model proposed by Maheswari, Kadono, and Ohtsu[12] for a random distribution of structures (oval defects in our case) on a surface. The PSD resulting from this model is

$$g(\mathbf{K}) \approx \rho |\hat{s}(\mathbf{K})|^2, \tag{15}$$

where ρ is the surface density of defects and $\hat{s}$ is the Fourier transform of the surface-defect profile $s(\mathbf{r})$. For identical defects, the PSD is thus given by the square modulus of the Fourier transform of a single defect (proportional to the defect height square). This function typically decays smoothly up to a certain spatial frequency, directly related with the defect lateral dimensions, where the PSD decays abruptly. If several distributions of defects are present, each with a characteristic defect size and density, the final PSD is obtained through the sum of the PSD associated with each particular distribution. In our sample, the oval defects show a broad dispersion of size and density, which indeed leads through averaging in Eq. (15) to a decorrelation of the PSD with respect to that of uniform distribution of defects; the resulting PSD consists of a monotonically decaying function with an abrupt roll-off at the frequency related to the minimum defect lateral size present on the surface. The decay rate of the PSD (the slope of the PSD in a linear fit of a log–log plot), which in sample C corresponds to a value $\gamma = -1.5$, will depend on each particular distribution of defect sizes and densities. The spatial frequency where we would expect a drop of the signal, as related to the defects of 100 nm (minimum defect size observed in sample C by AFM measurements), cannot be reached with our experimental setup.

Our results show that the GaAs layer roughness contribution to the PSD exceeds that of the defects at the low-spatial-frequency range, dominating PSD behavior. For larger spatial frequencies, a change in the PSD slope is detected, most likely indicating that the contribution from oval defects then becomes larger than that from the GaAs layer roughness. This reveals that, depending on their size and density, the contribution of oval defects to the PSD extends over a wide spatial-frequency range available for LLS measurements with visible light and may even be predominant. Therefore, care must be taken during *in situ* MBE LLS measurements because the light scattered from oval defects could mask the signal coming from other types of roughness, which could be our main interest. A test of AzLS behavior could be helpful to know the true origin of the scattered light. However, for good growth conditions and system cleanliness, the density of oval defects is highly reduced and its contribution to the PSD could be neglected.

V. SUMMARY AND CONCLUSIONS

In the preceding sections, we have analyzed typical morphologies of epitaxial III–V compound semiconductor layers, using the polarized laser light scattering (LLS) technique. In particular, we have studied $\mathrm{In}_{0.2}\mathrm{Ga}_{0.8}\mathrm{As}$ surfaces with crosshatched morphology, which typically develops during heteroepitaxial growth of III–V systems with small lattice mismatch ($\epsilon_0 < 2\%$). To study the influence of oval defects in the scattering pattern produced by different types of roughness, we have also analyzed a surface with a random distribution of these features.

From angle-resolved light scattering (ARLS) data, we have retrieved the power spectral density (PSD) by using a perturbation-theoretical model that appears to be adequate for the III–V heteroepitaxial systems under study. The PSDs thus obtained from data corresponding to both *s* and *p* polarizations and various angles of incidence exhibit excellent consistency, thus validating the approximations involved in the model.

One main conclusion is that the analysis of the PSD provides quantitative data on surface morphology, which agree with the AFM results.

We have considered the contribution of the presence of oval defects to the surface power spectral density. We have shown that the presence of a high density of oval defects must be considered, because it could mask the signal coming from another kind of roughness.

All of these results point out the high potential of LLS for use as an *in situ*, real-time technique for monitoring epitaxial growth processes. These results establish the limitations of the technique. Although the *in situ* extraction of the surface PSD has several geometrical constraints, the time evolution of scattered light at a fixed angular position together with AzLS measurements can still yield useful information. On the one hand, the increase of the scattered light indicates that the surface is roughening. On the other hand, *in situ* AzLS measurements give us key information about the degree of isotropy of the sample morphology, which is essential to assess the characteristics of the evolution of the growth front in real time.

We note the advantages of carrying out LLS experiments while varying the incident light wavelength,[23] as this over-comes the geometrical restrictions imposed by *in situ* measurements and allows us to retrieve the surface PSD, which is indispensable to obtain quantitative information on surface roughness. It is also worth mentioning that the use of ultraviolet light can increase the sensitivity toward high-spatial-frequency components (constrained by the Rayleigh limit). This can be a relevant factor in some cases in which one tries to detect small features, such as the formation of quantum dots[22] on semiconductor surfaces.

ACKNOWLEDGMENTS

The authors are very grateful to Dr. R. García and A. San Paulo for the AFM measurements. The authors wish to acknowledge the Spanish CICYT for financial support under Project No. TIC96-1020-C02. M.U.G. thanks the Consejería de Educación y Cultura de la Comunidad de Madrid for financial support. J.A.S.-G. acknowledges financial support from the Spanish DGESIC Grant No. PB97-1221.

[1] J. M. Benentt and L. Mattson, *Introduction to Surface Roughness and Scattering* (Optical Society of America, Washington, DC, 1989).
[2] J. A. Ogilvy, *Theory of Wave Scattering from Rough Surfaces* (Adam Hilger, Bristol, 1991).
[3] J. J. Greffet, Phys. Rev. B **37**, 6436 (1988).
[4] A. Duparré and S. Kassam, Appl. Opt. **32**, 5475 (1993).
[5] C. Amra, Appl. Opt. **32**, 5481 (1993).; J. Opt. Soc. Am. A **11**, 197, 211 (1994).
[6] J. A. Sánchez-Gil, A. A. Maradudin, J. Q. Lu, V. Freilikher, M. Pustilnik, and I. Yurkevich, Phys. Rev. B **50**, 15353 (1994).
[7] V. Freilikher, M. Pustilnik, I. Yurkevich, and V. I. Tatarskii, Opt. Lett. **19**, 1382 (1994).
[8] J. Q. Lu, J. A. Sánchez-Gil, E. R. Méndez , Z.-H. Gu, and A. A. Maradudin, J. Opt. Soc. Am. A **50**, 185 (1998).
[9] J. M. Elson, J. Opt. Soc. Am. A **12**, 729 (1995).
[10] R. G. Llamas and L. E. Regalado, Appl. Opt. **35**, 5583 (1996).
[11] J. A. Sánchez-Gil, A. A. Maradudin, and E. Méndez, J. Opt. Soc. Am. A **12**, 1547 (1995).
[12] R. U. Maheswari, H. Kadono, and M. Ohtsu, Opt. Commun. **131**, 133 (1996).
[13] T. Pinnington, C. Lavoie, T. Tiedje, B. Haveman, and E. Nodwell, Phys. Rev. Lett. **79**, 1698 (1997).
[14] K. L. Kavanagh, R. S. Goldman, C. Lavoie, B. Leduc, T. Pinnington, T. Tiedje, D. Klug, and J. Tse, J. Cryst. Growth **174**, 550 (1997).
[15] A. R. Boyd, T. B. Joyce, and R. Beanland, J. Cryst. Growth **164**, 51 (1996).
[16] D. J. Robbins, A. G. Cullis, and A. J. Pidduck, J. Vac. Sci. Technol. B **9**, 2048 (1991).
[17] U. Rossow, N. Dietz, K. J. Bachmann, and D. E. Aspnes, J. Vac. Sci. Technol. B **14**, 3040 (1996).
[18] C. T. Lee and Y. C. Chou, J. Cryst. Growth **91**, 169 (1988).
[19] A. A. Maradudin and T. R. Michel, J. Stat. Phys. **58**, 485 (1990).
[20] M. K. Nissen, C. Lavoie, S. Eisebitt, T. Pinnington, and T. Tiedje, Scanning Microsc. **8**, 935 (1994).
[21] V. A. Sterligov, Y. V. Subbota, Y. M. Shirshov, L. P. Pochekaylova, E. F. Venger, R. V. Konakova, and I. Y. Ilyin, Appl. Opt. **38**, 2666 (1999).
[22] T. Pinnington, Y. Levy, J. A. MacKenzie, and T. Tiedje, Phys. Rev. B **60**, 15901 (1999).
[23] E. Chason, M. B. Sinclair, J. A. Floro, J. A. Hunter, and R. Q. Hwang, Appl. Phys. Lett. **72**, 3276 (1998).